

Temperature-dependent structure and magnetization of $YCrO_3$ compound

Qian Zhao(赵前), Ying-Hao Zhu(朱英浩), Si Wu(吴思), Jun-Chao Xia(夏俊超),Peng-Fei Zhou(周鹏飞), Kai-Tong Sun(孙楷橦), and Hai-Feng Li(李海峰)

Citation: Chin. Phys. B, 2022, 31 (**4**): 046101. DOI: 10.1088/1674-1056/ac2b23

Journal homepage: http://cpb.iphy.ac.cn; http://iopscience.iop.org/cpb

What follows is a list of articles you may be interested in

Pressure dependence of the thermal stability in $LiMn_2O_4$

Yan Zeng(曾彦), Hao Liang(梁浩), Shixue Guan(管诗雪), Junpu Wang(王俊普), Wenjia Liang(梁文嘉), Mengyang Huang(黄梦阳), and Fang Peng(彭放)

Chin. Phys. B, 2022, 31 (**1**): 016104. DOI: 10.1088/1674-1056/ac1932

Compression behavior and phase transition of β-Si_3N_4 under high pressure

Hong-xia Gong(龚红霞), Zi-li Kou(寇自力), Cong Fan(樊聪), Hao Liang(梁浩), Qi-ming Wang(王齐明), Lei-lei Zhang(张雷雷), Fang Peng(彭放), Ming Yang(杨鸣), Xiao-lin Ni(倪小林), Jing Liu(刘景)

Chin. Phys. B, 2018, 27 (**5**): 056101. DOI: 10.1088/1674-1056/27/5/056101

Structural, magnetic properties, and electronic structure of hexagonal FeCoSn compound

Yong Li(李勇), Xue-Fang Dai(代学芳), Guo-Dong Liu(刘国栋), Zhi-Yang Wei(魏志阳), En-Ke Liu(刘恩克), Xiao-Lei Han(韩小磊), Zhi-Wei Du(杜志伟), Xue-Kui Xi(郗学奎), Wen-Hong Wang(王文洪), Guang-Heng Wu(吴光恒)

Chin. Phys. B, 2018, 27 (**2**): 026101. DOI: 10.1088/1674-1056/27/2/026101

Growth of PbS nanoclusters on specific sites of programmed oligodeoxynucleotides

Lu Ying, Teng Cui-Juan, Li Ying, Wang Hui, Xu Chun-Hua, Hu Shu-Xin, Li Ming

Chin. Phys. B, 2015, 24 (**1**): 016101. DOI: 10.1088/1674-1056/24/1/016101

Structural and magnetic properties of $BiFe_{1-x}Cr_xO_3$ synthesized samples

S. S. Arafat

Chin. Phys. B, 2014, 23 (**6**): 066101. DOI: 10.1088/1674-1056/23/6/066101

Temperature-dependent structure and magnetization of $YCrO_3$ compound

Qian Zhao(赵前)[1,2,†], Ying-Hao Zhu(朱英浩)[1,3,†], Si Wu(吴思)[1,3], Jun-Chao Xia(夏俊超)[1,3], Peng-Fei Zhou(周鹏飞)[1], Kai-Tong Sun(孙楷橦)[1], and Hai-Feng Li(李海峰)[1,‡]

[1] *Joint Key Laboratory of the Ministry of Education, Institute of Applied Physics and Materials Engineering, University of Macau, Avenida da Universidade, Taipa, Macao SAR* 999078, *China*

[2] *State Key Laboratory of High Performance Ceramics and Superfine Microstructure, Shanghai Institute of Ceramics, Chinese Academy of Sciences, Shanghai* 200050, *China*

[3] *Guangdong–Hong Kong–Macao Joint Laboratory for Neutron Scattering Science and Technology, Dongguan* 523803, *China*

(Received 23 August 2021; revised manuscript received 24 September 2021; accepted manuscript online 29 September 2021)

We have grown a $YCrO_3$ single crystal by the floating-zone method and studied its temperature-dependent crystalline structure and magnetization by x-ray powder diffraction and PPMS DynaCool measurements. All diffraction patterns were well indexed by an orthorhombic structure with space group of *Pbnm* (No. 62). From 36 K to 300 K, no structural phase transition occurs in the pulverized $YCrO_3$ single crystal. The antiferromagnetic phase transition temperature was determined as $T_N = 141.58(5)$ K by the magnetization versus temperature measurements. We found weak ferromagnetic behavior in the magnetic hysteresis loops below T_N. Especially, we demonstrated that the antiferromagnetism and weak ferromagnetism appear simultaneously upon cooling. The lattice parameters (a, b, c, and V) deviate downward from the Grüneisen law, displaying an anisotropic magnetostriction effect. We extracted temperature variation of the local distortion parameter Δ. Compared to the Δ value of Cr ions, Y, O1, and O2 ions show one order of magnitude larger Δ values indicative of much stronger local lattice distortions. Moreover, the calculated bond valence states of Y and O2 ions have obvious subduction charges.

Keywords: orthochromates, x-ray powder diffraction, crystal structure, magnetization

PACS: 61.05.C−, 61.50.Ah, 75.50.−y, 75.60.Ej **DOI:** 10.1088/1674-1056/ac2b23

1. Introduction

It is well known that structure symmetry and crystallographic environment are decisive factors in determining physical properties of materials.[1–4] Therefore, solving the crystal structure of perovskite transition-metal oxides with general formula of ABO_3 plays a pivotal role in shedding light on the mechanism of intriguing properties. For ideal ABO_3 compounds, the cubic crystal structure (space group: $Pm\bar{3}m$) is constructed by a 3D framework of corner-sharing octahedra with B cations accommodated at the center,[5] which generates crystal field splitting of the five-fold-degenerate 3d orbitals and splits the d-level into two-fold-degenerate e_g and three-fold-degenerate t_{2g} levels. With the symmetry breaking in a tetragonal crystal environment, distorted BO_6 octahedra further lift the two-fold e_g ($d_{x^2-y^2}$ and $d_{3z^2-r^2}$) and the three-fold t_{2g} (d_{xy}, d_{zx}, and d_{yz}) degeneracies.

Chemical pressure imposed by coordination of different A and B cations or by doping would result in some degrees of mismatch between the equilibrium A–O and B–O bond lengths. Consequently, the A ions will be inadequate for filling the space between BO_6 octahedra. Thus the structure symmetry lowers. This kind of distortion can be quantitatively reflected by the value of tolerance factor t.[6–8] An alternative to distorted BO_6 octahedra and lowered crystal structural symmetry is temperature variation. Therefore, temperature-dependent structural study is important for a full understanding of the novel physical properties such as multiferroics,[9] dielectrics,[10] thermoelectricity,[11] superconductivity,[12] and colossal magnetoresistance.[13,14]

Ferroelectric compounds are technologically interesting materials in data storage devices, catalysts, and sensors.[15–17] $YCrO_3$ is one of the most significant compounds in perovskite-type oxides due to its potential coexistence of ferroelectricity and magnetism and its high thermal, electrical, and structural stability.[6,18,19] This compound shows a coexistence of antiferromagnetism and weak ferromagnetism and displays a spin–phonon coupling.[20] A concept of 'local non-centrosymmetry' was proposed for the understanding of ferroelectricity observed in the centrosymmetric crystal structure of $YCrO_3$.[21] This is different from conventional ferroelectric systems. The local electric polarization of $YCrO_3$ single crystals grown by the flux method is along the c axis and the [110] direction in the *Pbnm* symmetry,[22] which depends on the direction of the applied electric field with respect to the crystal axes and was attributed to two types of local polar domains:

†These authors contributed equally.

‡Corresponding author. E-mail: haifengli@um.edu.mo

© 2022 Chinese Physical Society and IOP Publishing Ltd

One is with structural distortions forming near Pb^{2+} ions; the other is the magnetic phase separation domains forming near Pb^{4+} ions. Therefore, the introduction of impurity Pb^{2+} and Pb^{4+} ions in the crystallographic position of Y^{3+} sites results in the energetically beneficial processes of the formation of the local ferroelectric ordering in the isolated domains.[22] Unfortunately, the study did not find any homogeneous ferroelectric orders in $YCrO_3$ single crystals from 5 K to 350 K.[22] So far, the crystal structure of $YCrO_3$ has been determined to be orthorhombic with space group of *Pbnm*.[22,23] It was reported that $YCrO_3$ compound displays a canted antiferromagnetic (AFM) structure with antisymmetric spin superexchanges, and the weak ferromagnetism is along the *c* axis below T_N.[21,24–26] The ferroelectric relaxation was observed below $\sim$ 450 K.[10] However, the coupling mechanism of structure, ferroelectricity, and magnetism is still not clear. Previously, small single crystals of $YCrO_3$ were grown in millimeter size by the flux method,[22,27–29] however, impurities always exist.

In this paper, we have grown a centimeter-sized $YCrO_3$ single crystal with a laser-diode floating-zone (FZ) furnace[30] and performed a temperature-dependent x-ray powder diffraction (XRPD) study from 36 K to 300 K. We carried out magnetization measurements versus temperatures and applied magnetic fields with a PPMS DynaCool, with which we determined the onset temperature, T_N, of antiferromagnetism and observed weak ferromagnetism in the whole studied temperature regime below T_N. We refined the collected XRPD patterns and extracted crystallographic information such as lattice constants, unit-cell volume, local distortion parameter (Δ), bond valence states (BVSs), and isotropic thermal parameter (B). We found an anisotropic magnetostriction effect and subduction charges of Y and O2 ions.

2. Experimental details

The polycrystalline $YCrO_3$ samples were synthesized by a mixture of raw materials Y_2O_3 (ALFA AESAR, 99.9%) and Cr_2O_3 (ALFA AESAR, 99.6%) compounds with a mole ratio of 1:1.08 through solid-state reaction method.[8] Firstly, we mixed and ground the mixture of raw materials with a Vibrating Micro Mill (FRITSCH PULVERISETTE 0) for 1 h. Secondly, the mixture was heated in air at 1000 °C for 36 h with a temperature increasing/decreasing rate of 200 °C/h to perform the pre-reaction process. Thirdly, we performed a similar grinding, mixing, and heating procedure at 1200 °C for 36 h. After two cycles of calcination, we obtained a single-phase powder sample with green color. With additional treatments,[30] the powder sample was isostatically pressed into a cylindrical rod of $\sim$ 12 cm long under a pressure of $\sim$ 70 MPa. The rod was then sintered in air at 1350 °C for 36 h. Through the above firing steps and grinding and mixing with a 50 mm diameter ball after each heating process, we finally prepared a dense and uniform sample.[31] The single crystals of $YCrO_3$ compound were grown by the FZ method[8] with a laser-diode FZ furnace (Model: LD-FZ-5-200W-VPO-PC-UM).[30,32]

We chose shiny pieces of $YCrO_3$ single crystals and carefully pulverized them into powder samples with a Vibratory Micro Mill and performed a XRPD study from 36 K to 300 K with a 2θ range of 24°–89° and a step size of 0.005° on an in-house x-ray diffractometer (Rigaku, SmartLab 9 kW) employing copper $K_{\alpha1}$ (1.54056 Å) and $K_{\alpha2}$ (1.54439 Å) with a ratio of 2:1 as the radiation. XRPD patterns were collected at a voltage of 45 kV and a current of 200 mA at ambient conditions. The collected XRPD patterns were refined with the software of FULLPROF SUITE.[33] We refined the scale factor, lattice constants, background, peak profile shape, atomic positions, isotropic thermal parameter, and preferred orientation for following analyses. The magnetization measurements of a $YCrO_3$ single crystal were performed on a Quantum Design physical property measurement system (PPMS DynaCool instrument). The dc magnetization measurements at an applied magnetic field of 20 Oe were carried out with two modes from 1.8 K to 350 K: One was after cooling down with zero magnetic field (ZFC), and the other was with the applied magnetic field while cooling (FC). Magnetic hysteresis loops were measured from 0 to 14 T, then to -14 T, and finally back to 14 T with temperatures at 5 K, 90 K, and 135 K.

3. Results and discussion

3.1. X-ray powder diffraction

In order to explore possible structural phase transitions in the pulverized $YCrO_3$ single crystal at low temperatures, we carried out XRPD measurements with increasing temperature from 36 K to 300 K. The representative XRPD patterns as well as the corresponding structural refinements are shown in Fig. 1. The $YCrO_3$ compound undergoes an AFM phase transition[34] at $T_N = 141.58(5)$ K. Below T_N, it enters into a canted AFM state. Therefore, we chose three temperature points 40 K (below T_N), 150 K (around T_N), and 300 K (above T_N) for the XRPD study. We indexed all collected data with an orthorhombic structure and a space group of *Pbnm* (No. 62). We carefully checked the Bragg peak shape and positions, especially for the reflections locating at higher 2θ degrees. No impurity peaks and detectable peak splitting were observed. This indicates that there is no structural phase transition occurring in the pulverized $YCrO_3$ single crystal in the whole studied temperature range within the present experimental resolution. The small difference between collected and calculated

XRPD patterns (Fig. 1) and the low values of goodness of fit (Table 1) further validate our refinements. The refined unit-cell of the orthorhombic structure is exhibited in Fig. 2, and all extracted crystallographic information at 40 K, 150 K, and 300 K is listed in Table 1.

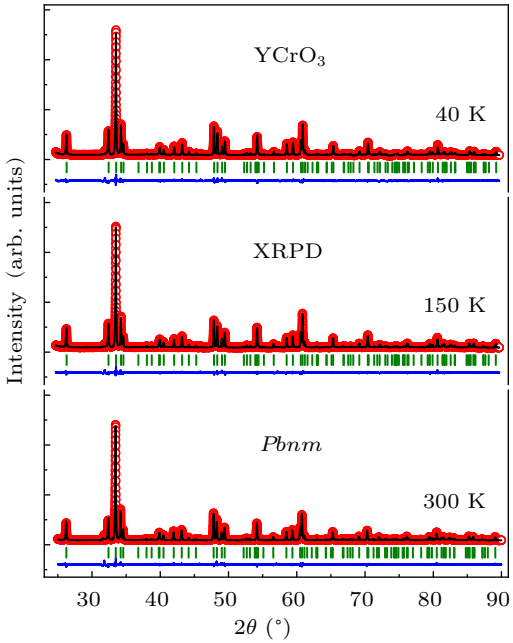


Fig. 1. Observed (circles) and calculated (solid lines) XRPD patterns of a pulverized $YCrO_3$ single crystal, collected at 40 K, 150 K, and 300 K. The vertical bars mark the positions of Bragg reflections, and the lower curves represent the difference between observed and calculated patterns.

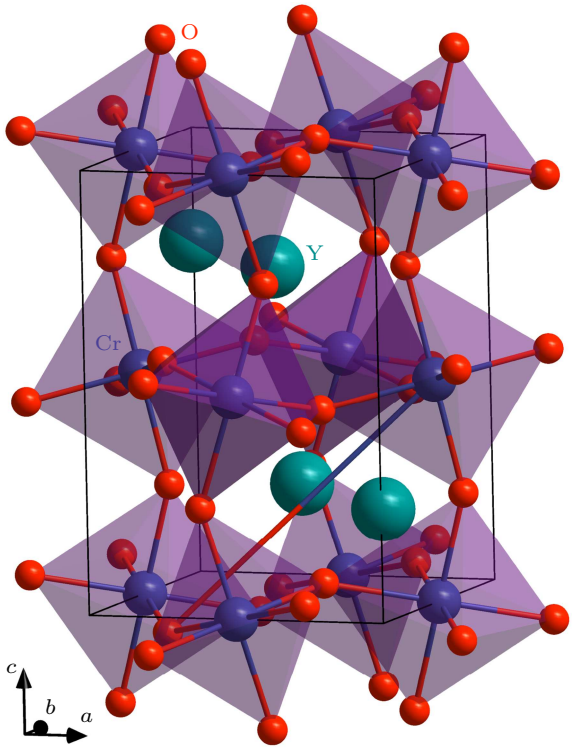


Fig. 2. Orthorhombic crystal structure (space group: *Pbnm*) with one unit cell (solid lines) of a $YCrO_3$ single crystal at 300 K. The CrO_6 octahedra are highlighted in purple.

Table 1. Refined structural parameters of a pulverized $YCrO_3$ single crystal at 40 K, 150 K, and 300 K, including lattice constants, unit-cell volume, atomic positions, isotropic thermal parameter (B), bond lengths, and the distortion parameter Δ. We listed the Wyckoff site of each ion and the goodness of fit. The numbers in parenthesis are the estimated standard deviations of the (next) last significant digit.

A pulverized $YCrO_3$ single crystal (orthorhombic, space group *Pbnm* (No. 62), $Z = 4$)			
T (K)	40	150	300
a (Å)	5.23006(6)	5.23243(6)	5.23942(7)
b (Å)	5.51712(7)	5.51869(6)	5.52065(7)
c (Å)	7.51809(9)	7.52229(8)	7.53183(9)
$\alpha(=\beta=\gamma)$ (°)	90	90	90
V (Å^3)	216.934(5)	217.215(4)	217.858(5)
Y(4c) x	−0.01692(16)	−0.01687(14)	−0.01757(17)
Y(4c) y	0.06630(8)	0.06707(8)	0.06649(9)
Y(4c) z	0.25	0.25	0.25
Y(4c) B (Å^2)	2.510(21)	2.356(19)	2.946(23)
Cr(4b) (x,y,z)	(0.5, 0, 0)	(0.5, 0, 0)	(0.5, 0, 0)
Cr(4b) B (Å^2)	2.410(32)	2.617(30)	3.390(37)
O1(4c) x	0.11055(55)	0.11940(52)	0.10283(61)
O1(4c) y	0.45949(55)	0.46754(52)	0.46804(59)
O1(4c) z	0.25	0.25	0.25
O1(4c) B (Å^2)	1.683(55)	1.489(51)	2.701(64)
O2(8d) x	−0.31168(43)	−0.31187(40)	−0.31179(47)
O2(8d) y	0.30031(45)	0.30311(42)	0.29542(52)
O2(8d) z	0.05282(31)	0.05345(29)	0.05465(35)
O2(8d) B (Å^2)	1.683(55)	1.489(51)	2.701(64)
Y–O11 (Å)	2.2694(33)	2.3220(28)	2.3046(34)
Y–O12 (Å)	2.2058(33)	2.1511(27)	2.2401(33)
Y–O21 (Å) (×2)	2.4983(24)	2.5034(22)	2.4774(29)
Y–O22 (Å) (×2)	2.2705(25)	2.2610(23)	2.2810(29)
⟨Y–O⟩ (Å)	2.3355(11)	2.3336(10)	2.3436(12)
Cr–O1 (Å) (×2)	1.9790(10)	1.9897(9)	1.9664(9)
Cr–O21 (Å) (×2)	1.9678(26)	1.9819(22)	1.9498(27)
Cr–O22 (Å) (×2)	2.0072(23)	2.0014(21)	2.0284(27)
⟨Cr–O⟩ (Å)	1.9847(9)	1.9910(7)	1.9815(9)
Δ(Y) ($\times10^{-4}$)	25.264	31.105	16.950
Δ(Cr) ($\times10^{-4}$)	0.699	0.163	2.916
Δ(O1) ($\times10^{-4}$)	38.737	42.289	53.244
Δ(O2) ($\times10^{-4}$)	96.382	95.177	91.470
R_p	3.14	2.99	3.05
R_{wp}	4.57	4.28	4.68
R_{exp}	2.88	2.85	2.90
χ^2	2.53	2.26	2.61

3.2. Magnetization

Figure 3 shows the magnetization versus temperature of a small $YCrO_3$ single crystal. We converted the unit of the vertical axis to μ_B per Cr^{3+} ion. The difference between ZFC and FC data is probably caused by the movement of magnetic domain walls instead of a spin-glass like transition.[35] Upon cooling, the ZFC and FC magnetization curves remain extremely small until $\sim$ 141.58(5) K, around which the two curves increase simultaneously and sharply in a small temperature range of $\sim$ 5 K. With further cooling down to 1.8 K, a smooth increase appears in the FC curve, whereas an almost linear drop occurs in the ZFC curve. This indicates

a reasonable canted AFM phase transition. At 1.8 K, ZFC magnetization = $1.02(1) \times 10^{-3}$ μ_B/Cr^{3+}.

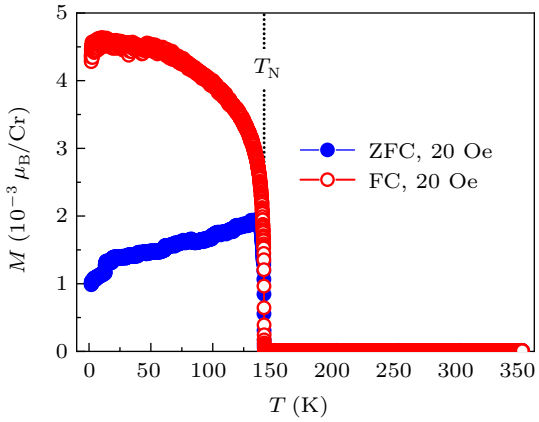


Fig. 3. Temperature dependence of the ZFC and FC magnetization (M) of chromium ions in a $YCrO_3$ single crystal measured at $B = 20$ Oe.

Figure 4(a) shows the measurements of magnetic hysteresis loop at 5 K, 90 K, and 135 K. Figure 4(b) displays clearly the narrow quasi-parallelogram hysteresis loops in applied magnetic field range of ~ -0.1 T to 0.1 T. At 5 K, a coercive force of ~ 84.26 Oe and a residual magnetization of $\sim 1.19(2) \times 10^{-2}$ μ_B/Cr^{3+} were determined. An increase of temperature to 90 K or 135 K diminishes the coercive force and the residual magnetization. The observed loops resemble the characteristic features of a soft ferromagnet at low temperatures. Thus there exists a coexistence of AFM and weak ferromagnetic behaviors in $YCrO_3$ below $T_N \sim 141.58(5)$ K.

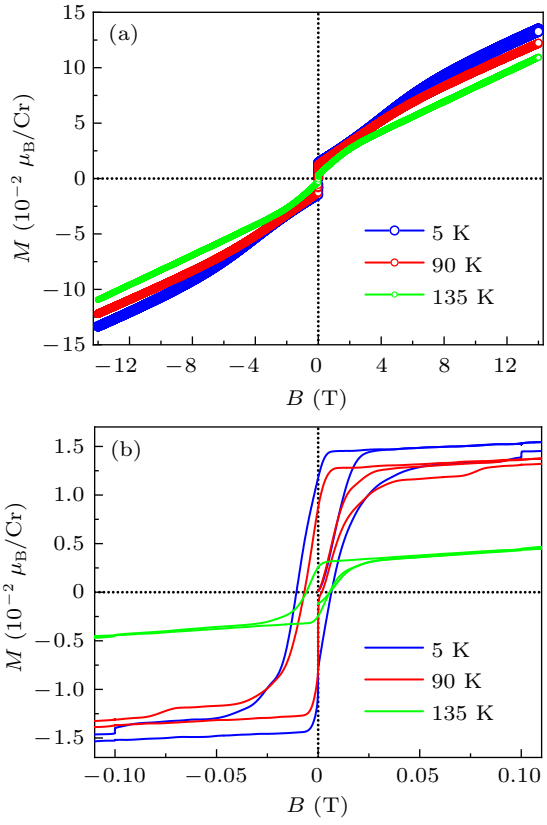


Fig. 4. (a) Magnetic hysteresis loops of a $YCrO_3$ single crystal measured in a field range of -14 T to 14 T at 5 K, 90 K, and 135 K. (b) For a clear comparison, we displayed the loops in a narrow field regime.

3.3. Anisotropic magnetostriction effect

The refined lattice parameters a, b, and c from our XRPD studies are shown as void symbols in Fig. 5. The corresponding change in unit-cell volume V is depicted in Fig. 6. As is well known, the $YCrO_3$ compound is an insulator.[34] Thus the contribution of electrons to the thermal expansion of lattice parameter (ε) can be neglected. The non-magnetic contribution to the thermal expansion is then mainly from phonons. Thus it can be approximately estimated according to the Grüneisen rules at zero pressure with a second-order form,[36–38] i.e.,

$$\varepsilon(T) = \varepsilon_0 + \varepsilon_0 \frac{U}{Q - BU}, \tag{1}$$

where ε_0 is the lattice parameter at 0 K, and the internal energy U can be calculated with the Debye approximations[34]

$$U(T) = 9Nk_BT\left(\frac{T}{\Theta_D}\right)^3 \int_0^{\frac{\Theta_D}{T}} \frac{x^3}{e^x - 1}\,dx, \tag{2}$$

where $N = 5$ is the number of atoms per formula unit, and $\Theta_D = 580$ K is the Debye temperature.[31] With Eqs. (1) and (2), we fit the lattice parameters of $YCrO_3$ in a temperature range of 150–300 K (in the paramagnetic state) and extrapolate the fits to overall temperatures shown as solid lines in Figs. 5 and 6. The values of the fitting parameters of ε_0, Q, and B are listed in Table 2. It is obvious that below T_N, the fitting to the unit-cell volume deviates gradually from the refined values (Fig. 6). Differences exist between refined values

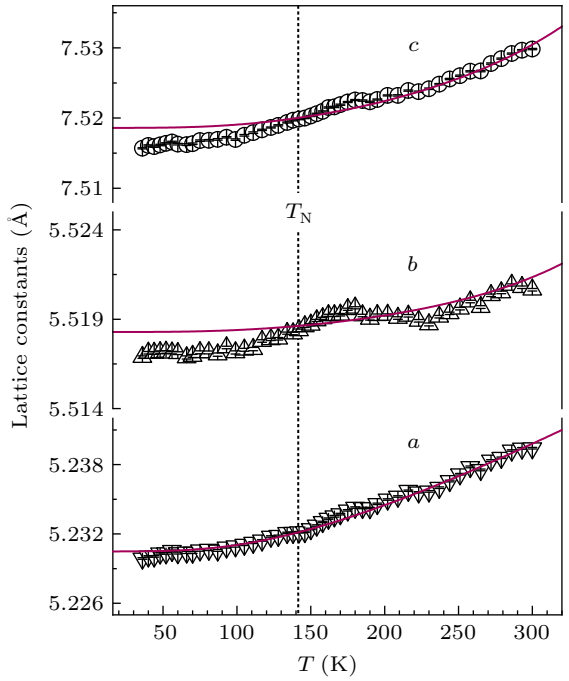


Fig. 5. Temperature-dependent lattice constants a, b, and c of a pulverized $YCrO_3$ single crystal (void symbols), which was extracted from our refinements based on the XRPD data collected from 36 K to 300 K. The solid lines are theoretical estimates of the variation of structural parameters using the Grüneisen model as discussed in the text with a Debye temperature $\Theta_D = 580$ K. The data was fit in paramagnetic state and extrapolated to overall temperature range. T_N labels the AFM transition temperature. Error bars are the standard deviations obtained from the refinements.

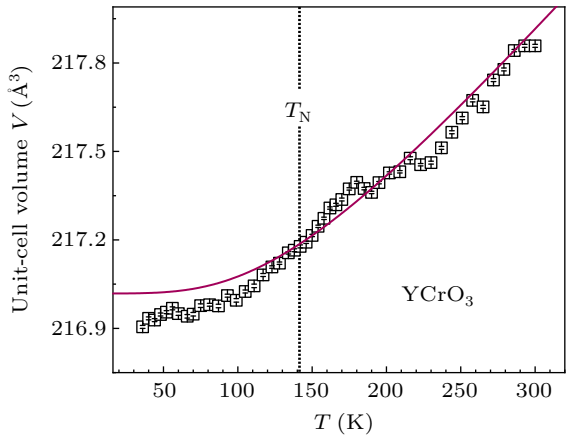


Fig. 6. Temperature-dependent unit-cell volume, V, extracted from the refinements. The solid line is theoretical estimate of the variation of unit-cell volume using the Grüneisen model. We fit the data in paramagnetic state and extrapolate to overall temperature range. The vertical short-dotted line implies the AFM transition temperature T_N. Error bars are the standard deviations obtained from the refinements.

of lattice constants a, b, and c and the corresponding theoretical estimates (Fig. 5), e.g., $\frac{a_{Re}^{36K}-a_{Gr}^{36K}}{a_{Gr}^{36K}} = -1.2(1)\times10^{-4}$, $\frac{b_{Re}^{36K}-b_{Gr}^{36K}}{b_{Gr}^{36K}} = -2.6(1)\times10^{-4}$, and $\frac{c_{Re}^{36K}-c_{Gr}^{36K}}{c_{Gr}^{36K}} = -3.9(1)\times10^{-4}$. Therefore, a magnetostriction effect exists in $YCrO_3$, that is, the magnetic phase transition affects the thermal expansion of the lattice parameters. In addition, the effect is anisotropic. Below T_N, the magnetically-driven additional decreases of a, b, and c jointly result in an extra contraction of the sample upon cooling, e.g., $\frac{V_{Re}^{36K}-V_{Gr}^{36K}}{V_{Gr}^{36K}} = -5.3(2)\times10^{-4}$.

Table 2. Values of the fitting parameters while estimating a, b, c, and V of $YCrO_3$ compound with Eqs. (1) and (2) in a temperature range of 150–300 K (Figs. 5 and 6). The numbers in parenthesis are the estimated standard deviations of the last significant digit.

Parameter (unit)	ε_0 (Å/Å^3)	Q (J)	B
a	5.23048(8)	$1.62(1)\times10^{-17}$	13.42(6)
b	5.51828(6)	$9.04(2)\times10^{-17}$	1407.68(7)
c	7.52059(8)	$2.89(8)\times10^{-17}$	393.37(4)
V	217.018(2)	$6.54(7)\times10^{-18}$	−9.79(7)

3.4. Local distortions of Y, Cr, and O ions

Local crystalline environment can be quantitatively evaluated by the distortion parameter Δ,[8,13,14,39] i.e.,

$$\Delta = \frac{1}{n}\sum_{i=1}^{n}\left(\frac{d_i - \langle d\rangle}{\langle d\rangle}\right)^2, \quad (3)$$

where n is the coordination number, d_i is the bond length along one of the n coordination directions, and $\langle d\rangle$ is the average bond length. We calculated the local distortion parameter Δ versus temperature for Y, Cr, O1, and O2 ions as shown in Fig. 7. In principle, there is no Jahn–Teller effect for Cr^{3+} ions. The calculated local distortion parameter Δ of Cr^{3+} ions keeps almost a constant of $\sim 1.04329\times10^{-4}$ in the whole studied temperature range. By contrast, Y, O1, and O2 ions have much larger Δ values, more than one order of magnitude larger than that of Cr ions. For example, at 40 K, $\Delta(O2) \approx 2.48\Delta(O1) \approx 3.81\Delta(Y) \approx 137.88\Delta(Cr)$, indicating that there are significant local distortions of Y, O1, and O2 ions, which could break the local centrosymmetry and produce geometric ferroelectricity.

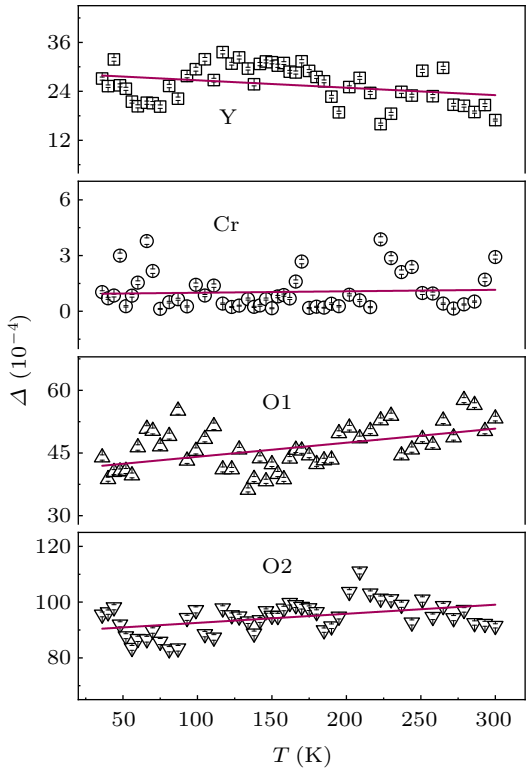


Fig. 7. Temperature variation of the distortion parameter, Δ, of Y, Cr, O1, and O2 ions of a single-crystal $YCrO_3$ (void symbols) from 36 K to 300 K. Error bars are the standard deviations obtained from the refinements. The solid lines are tentative linear fits.

3.5. Bond valence states of Y, Cr, and O ions

BVSs are defined as the classical valence shared with each bond.[40] From the refinements, we extracted the BVSs of Y, Cr, and O ions as shown in Fig. 8. The BVSs of Y and O ions almost decrease linearly as the temperature increases, whereas that of Cr ions nearly increases linearly. In the whole studied temperature range, the BVS of Y ions is largely smaller than 3+, and that of O2 ions is much larger than 2−. Therefore, it is clear that Y and O2 ions show subduction charges. We calculated the average BVS values of Cr and O1 ions, i.e., 2.958(7)+ and 2.093(7)−, respectively. By contrast, the average BVS values of Y and O2 ions are 2.661(9)+ and 1.763(6)−. They deviate largely from the ideal values of 3+ (for Y ions) and 2− (for O2 ions). The two nonequivalent O1 and O2 ions show a charge difference ~ 0.330 e$^-$ indicative of a big charge disproportion.

Figure 9 shows the temperature-dependent values of isotropic thermal parameter B of Y, Cr, and O1/O2 ions. During refinements, we constrained B(O1) to be same as B(O2). The parameter B is called Debye–Waller factor or temperature factor, describing the attenuation of diffraction intensity caused by the thermal motion of regularly-arranged electrons in x-ray diffraction. As temperature increases, the B values

of Y (from 150 K to 300 K), Cr, and O1/O2 ions (the whole temperature range) almost increase linearly (Fig. 9). This is consistent with the decrease in the x-ray diffraction intensities of Bragg peaks as shown in Fig. 1. It is noted that blow $\sim$ 150 K, the B values of Y ions have no obvious changes.

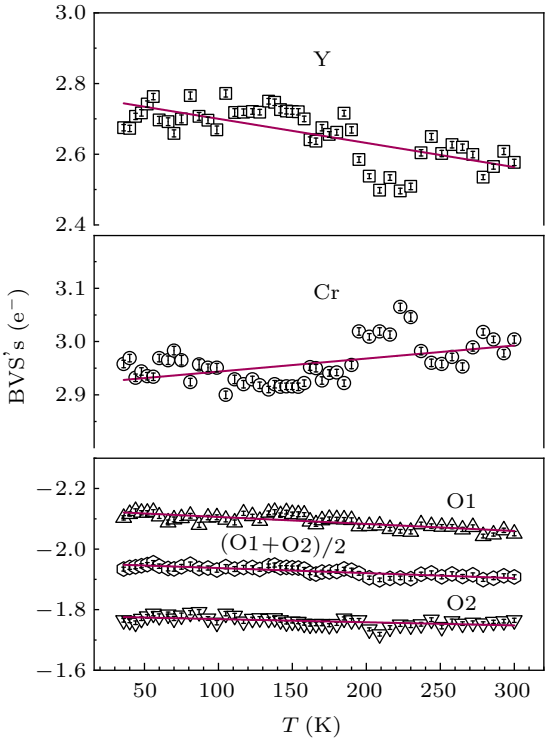


Fig. 8. Temperature variation of the bond valence states of Y, Cr, O1, and O2 ions of a single-crystal $YCrO_3$ from 36 K to 300 K (void symbols). We calculated the average bond valence states of O1 and O2 ions, i.e., (O1+O2)/2. Error bars are the (propagated) standard deviations.

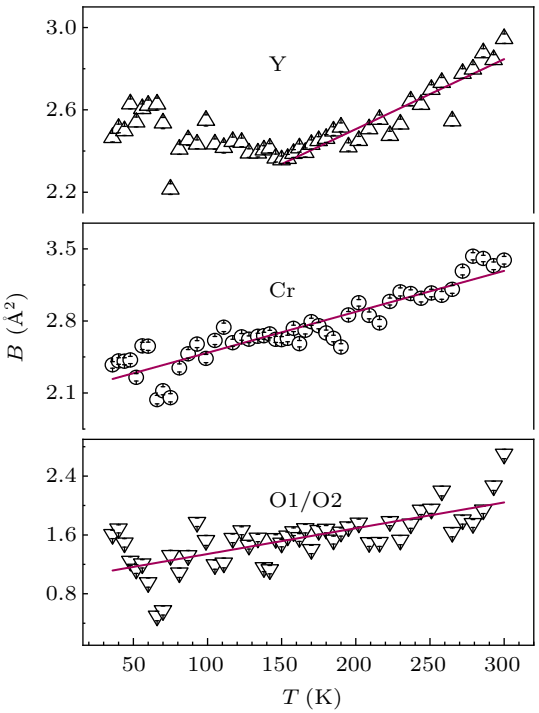


Fig. 9. Temperature variation of the isotropic thermal parameters, B, of Y, Cr, and O1/O2 ions of a single-crystal $YCrO_3$ (void symbols). During refinements, we constrained the B values of O1 and O2 ions as the same. Error bars are standard deviations obtained from the refinements.

It is stressed that the space group *Pbnm* belongs to a centrosymmetric point group that has an inversion center. All building elements display inversion symmetry. Therefore, in such a space group, no net polar forms, thus no ferroelectricity appears. We observed much larger local distortions of Y, O1, and O2 ions and clear subduction charges of Y and O2 ions, therefore, we infer that there may exist local noncentrosymmetric domains. This could be the origin of the reported ferroelectricity observed in $YCrO_3$ compound.

4. Conclusions

In summary, we carried out a detailed temperature-dependent XRPD study on a pulverized $YCrO_3$ single crystal grown by a laser-diode FZ technique. In the whole studied temperature range of 36–300 K, we did not find any crystalline structural phase transitions and thus indexed all collected XRPD patterns with an orthorhombic structure. By FULLPROF refinements, we extracted structure parameters of lattice constants, unit-cell volume, atomic positions, bond lengths, local distortions, BVSs, and thermal factors. We determined the AFM phase transition temperature $T_N = 141.58(5)$ K by the temperature-dependent magnetization study and found the weak ferromagnetism with the observation of magnetic hysteresis loops from 5 K to 135 K. We observed an anisotropic magnetostriction effect below the AFM phase transition temperature as demonstrated by the deviations of lattice parameters (a, b, c, and V) from the Grüneisen law. The local distortions (Δ) of Y, O1, and O2 ions are much larger than that of Cr ions. We found that both Y and O2 ions display large charge displacements from theoretical values of $3+$ and $2-$, respectively. We suggest that local distortions of Y and O2 ions could be the reason for the observed ferroelectric characteristic in $YCrO_3$ compound.

Acknowledgements

Authors acknowledge the opening project of State Key Laboratory of High Performance Ceramics and Superfine Microstructure (Grant No. SKL201907SIC), Science and Technology Development Fund, Macao SAR, China (File Nos. 0090/2021/A2 and 0051/2019/AFJ), Guangdong Basic and Applied Basic Research Foundation, China (Guangdong–Dongguan Joint Fund No. 2020B1515120025), University of Macau (MYRG2020-00278-IAPME and EF030/IAPME-LHF/2021/GDSTIC), and Guangdong–Hong Kong–Macao Joint Laboratory for Neutron Scattering Science and Technology (Grant No. 2019B121205003).

References

[1] Wang K, Qi Q, Cheng G J and Shi L Q 2014 *Chin. Phys. Lett.* **31** 072801
[2] Zhang H, Luo J, Zhu H T, Liu Q L, Liang J K and Rao G H 2012 *Acta Phys. Sin.* **61** 086101 (in Chinese)

[3] Zhang B, An C, Zhou Y, Chen X, Zhou Y, Chen C, Yuan Y and Yang Z 2019 *Chin. Phys. B* **28** 126202
[4] Wang M, Shen W S, Li X D, Li Y C, Zhang G Z, Liu C L, Zhao L, Lü S P, Gao C X and Han Y H 2019 *Chin. Phys. B* **28** 076109
[5] Ardit M, Cruciani G, Dondi M, Merlini M and Bouvier P 2010 *Phys. Rev. B* **82** 064109
[6] Looby J T and Katz L 1954 *J. Am. Chem. Soc.* **76** 6029
[7] Kumar A, Verma A S and Bhardwaj S R 2008 *The Open Applied Physics Journal* **1** 11
[8] Li H F 2008 *Synthesis of CMR manganites and ordering phenomena in complex transition metal oxides* (Forschungszentrum Juelich GmbH Press)
[9] Fiebig M, Lottermoser T, Fröhlich D, Goltsev A V and Pisarev R V 2002 *Nature* **419** 818
[10] Serrao C R, Kundu A K, Krupanidhi S, Waghmare U V and Rao C 2005 *Phys. Rev. B* **72** 220101
[11] Okuda T, Nakanishi K, Miyasaka S and Tokura Y 2001 *Phys. Rev. B* **63** 113104
[12] Cava R, Batlogg B, Krajewski J, Farrow R, Rupp L J, White A, Short K, Peck W and Kometani T 1988 *Nature* **332** 814
[13] Li H, Su Y, Persson J, Meuffels P, Walter J, Skowronek R and Brückel T 2006 *J. Phys.: Condens. Matter* **19** 016003
[14] Li H, Su Y, Persson J, Meuffels P, Walter J, Skowronek R and Brückel T 2007 *J. Phys.: Condens. Matter* **19** 176226
[15] Auciello O, Scott J F and Ramesh R 1998 *Physics Today* **51** 22
[16] Van Aken B B, Palstra T T, Filippetti A and Spaldin N A 2004 *Nat. Mater.* **3** 164
[17] Zhao H J, Ren W, Yang Y R, Íñiguez J, Chen X M and Bellaiche L 2014 *Nat. Commun.* **5** 4021
[18] Chakraborty P and Basu S 2021 *Materials Chemistry and Physics* **259** 124053
[19] Levin E M and McMurdie H F 1975 *Phase diagrams for ceramists*, 1975 supplement (United States: American Ceramic Society, Inc., Columbus, OH)
[20] Sharma Y, Sahoo S, Perez W, Mukherjee S, Gupta R, Garg A, Chatterjee R and Katiyar R S 2014 *J. Appl. Phys.* **115** 183907
[21] Ramesha K, Llobet A, Proffen T, Serrao C and Rao C 2007 *J. Phys.: Condens. Matter* **19** 102202
[22] Sanina V, Khannanov B K, Golovenchits E and Shcheglov M 2018 *Physics of the Solid State* **60** 2532
[23] Geller S and Wood E 1956 *Acta Crystallographica* **9** 563
[24] Jüdin V and Sherman A 1966 *Solid State Commun.* **4** 661
[25] Bertaut E, Bassi G, Buisson G, *et al.* 1966 *J. Appl. Phys.* **37** 1038
[26] Morishita T and Tsushima K 1981 *Phys. Rev. B* **24** 341
[27] Remeika J 1956 *J. Am. Chem. Soc.* **78** 4259
[28] Grodkiewicz W and Nitti D 1966 *Journal of the American Ceramic Society* **49** 576
[29] Todorov N, Abrashev M, Ivanov V, Tsutsumanova G, Marinova V, Wang Y Q and Iliev M 2011 *Phys. Rev. B* **83** 224303
[30] Li H F, Zhu Y H, Wu S and Tang Z K 2021 China Patent No. CN110904497B [2021-06-11]
[31] Zhu Y, Wu S, Tu B, *et al.* 2020 *Phys. Rev. B* **101** 014114
[32] Wu S, Zhu Y, Gao H, *et al.* 2020 *ACS omega* **5** 16584
[33] Rodríguez-Carvajal J 1993 *Physica B* **192** 55
[34] Zhu Y, Fu Y, Tu B, *et al.* 2020 *Phys. Rev. Materials* **4** 094409
[35] Chang H, Guo Y Q, Liang J K and Rao G H 2004 *J. Magn. Magn. Mater.* **278** 306
[36] Li H F, Xiao Y G, Schmitz B, Persson J, Schmidt W, Meuffels P, Roth G and Brückel Th 2012 *Sci. Rep.* **2** 750
[37] Wallace D C 1998 *Phys. Rev. B* **58** 15433
[38] Vočadlo L, Knight K, Price G and Wood I 2002 *Physics and Chemistry of Minerals* **29** 132
[39] Li H F, Su Y, Xiao Y, Persson J, Meuffels P and Brückel T 2009 *Euro. Phys. J. B* **67** 149
[40] Mohri F 2000 *Acta Crystallographica Section B: Structural Science* **56** 626